RESEARCH ARTICLE

Key Points:
- No phase transitions were observed in Ti-bearing clinohumite up to 28 GPa and 750 K
- Ti-poor and Ti-rich clinohumites display similar equations of state but are ~20% more incompressible than Mg-pure clinohumite
- High-pressure high-temperature properties of Ti-bearing clinohumite will improve mineralogical models of volatile and HFSE fluxes in the crust-mantle system

Thermal Equation of State of Natural Ti-Bearing Clinohumite

Fei Qin[1,2] (ID)**, Xiang Wu[3]** (ID)**, Dongzhou Zhang[4]** (ID)**, Shan Qin[1]** (ID)**, and Steven D. Jacobsen[2]** (ID)

[1]Key Laboratory of Orogenic Belts and Crustal Evolution, MOE, Peking University and School of Earth and Space Sciences, Peking University, Beijing, China, [2]Department of Earth and Planetary Sciences, Northwestern University, Evanston, IL, USA, [3]State Key Laboratory of Geological Processes and Mineral Resources, China University of Geosciences, Wuhan, China, [4]School of Ocean and Earth Science and Technology, Hawai'i Institute of Geophysics and Planetology, University of Hawaii at Mānoa, Honolulu, HI, USA

Abstract The natural occurrence of clinohumite in metabasalts and hydrothermally altered peridotites provides a source of water-rich minerals in subducted slabs, making knowledge of their phase relations and crystal chemistry under high pressure-temperature (*P-T*) conditions important for understating volatile recycling and geodynamic process in the Earth's mantle. Here we present a synchrotron-based, single-crystal X-ray diffraction study on two natural Ti-bearing clinohumites up to ~28 GPa and 750 K in order to simulate conditions within subducted slabs. No phase transition occurs in clinohumite over this *P-T* range. Pressure-volume relationships of both compositions at room temperature were fitted to a third-order Birch-Murnaghan equation of state (EoS) with $V_0 = 650.4(3)$ Å^3, $K_{T0} = 141(4)$ GPa, and $K_{T0}' = 4.0(6)$ for Ti-poor clinohumite (0.07 Ti per formula unit, pfu) and $V_0 = 650.8(3)$ Å^3, $K_{T0} = 144(4)$ GPa, and $K_{T0}' = 3.6(7)$ for Ti-rich clinohumite (0.21 Ti pfu). Both clinohumites exhibit anisotropic compression with $\beta_b > \beta_c > \beta_a$. We also refined *P-V-T* equation of state parameters using the high-temperature Birch-Murnaghan EoS, yielding $(\partial K_{T0}/\partial T)_P = -0.040(10)$ GPa/K and $\alpha_T = 5.1(6) \times 10^{-5}$ K^{-1} for Ti-poor clinohumite and $(\partial K_{T0}/\partial T)_P = -0.045(11)$ GPa/K and $\alpha_T = 5.7(6) \times 10^{-5}$ K^{-1} for Ti-rich clinohumite. Ti-poor and Ti-rich clinohumites display similar equations of state but are ~20% more incompressible than Mg-pure clinohumite and display ~5% higher bulk sound velocity than olivine at upper mantle conditions. Our results provide constraints for modeling geodynamic process related to the subduction and transport of potentially water-rich slabs in the mantle.

1. Introduction

Water, transported into the deep mantle via hydrous minerals in subducted slabs, can affect many chemical and physical properties of mantle materials including elasticity, rheology, electrical conductivity, and other transport properties (Hirth & Kohlstedt, 1996; Jacobsen & Smyth, 2006; Karato & Wu, 1993; Mao & Li, 2016; Yoshino et al., 2009). The recycling of water in the crust-mantle system has significant implications for understanding geochemical and geodynamical evolutions of the Earth (Faccenda, 2014; Hirschmann, 2006; Ohtani, 2005). The discovery of a natural water-rich ringwoodite (1.4 wt % H$_2$O) included in diamond implies that some regions of the Earth's transition zone could be very hydrous (Pearson et al., 2014) and there is evidence for dehydration melting both above and below the transition zone discontinuities (Hier-Majumder & Tauzin, 2017; Liu et al., 2016; Schmandt et al., 2014). Minerals that can transport water into the transition zone have therefore been studied extensively in the MgO-SiO$_2$-H$_2$O system, where dense hydrous magnesium silicates (DHMSs) are regarded as primary candidates (Ohtani et al., 2000).

Subducted slabs not only transport water into the mantle but are also enriched in large-ion lithophile elements (LILEs), light rare earth element (LREE)-bearing phases such as epidote and lawsonite (Qin et al., 2016), together with high field strength elements (HFSE) and related Ti-rich minerals (Scambelluri & Philippot, 2001). The natural occurrence of Ti-rich humite-group minerals in metabasalts and hydrothermally altered peridotites makes knowledge of their phase relations and crystal chemistry under high *P-T* conditions relevant to understanding geochemical cycling in the crust-mantle system (Scambelluri & Rampone, 1999).

Humite minerals include a series of magnesium orthosilicates with structures based on a slightly distorted hexagonal close packed arrays of anions (O, F, and OH) with one-half of the octahedral sites occupied by M cations and 8–12% of the octahedral sites occupied by Si. A general humite formula may be written, nM$_2$SiO$_4$·M$_{1-x}$Ti$_x$(F,OH)$_{2-2x}$O$_{2x}$, where M is Mg with minor amounts ($x < 0.5$) of Ti, Fe^{2+}, Mn, Ca, etc. and $n = 1$ for norbergite, 2 for chondrodite, 3 for humite, and 4 for clinohumite. Within the humite group,

clinohumite and chondrodite possess the highest *P-T* stability (Friedrich et al., 2002). Previous studies have reported the room temperature compressibility or room-pressure thermal expansivity of humite minerals using X-ray diffraction (Ross & Crichton, 2001; Ye et al., 2013, 2015). The OH environments in clinohumite and chondrodite have been studied by infrared spectroscopy (Liu et al., 2003; Prasad & Sarma, 2004), as well as Raman spectroscopic and neutron diffraction studies of norbergite, clinohumite, and chondrodite (Friedrich et al., 2001, 2002; Lin et al., 2000, 1999; Ye et al., 2015, 2013). Ross and Crichton (2001) studied the compressibility of single-crystal clinohumite up to 8.1 GPa, resulting in $K_T = 119.4(7)$ GPa and $K_T' = 4.8(6)$ for synthetic and Mg-pure hydroxylclinohumite. By comparison with other phases along the forsterite-brucite join (e.g., hydroxylchondrodite and phase A), a roughly linear relationship can be observed between water content and bulk modulus (Ross & Crichton, 2001; Ye et al., 2015). The elastic properties of hydroxylclinohumite have also been investigated using Brillouin spectroscopy by Fritzel and Bass (1997), who reported 125(2) GPa for the adiabatic bulk modulus and 73(5) GPa for the shear modulus of an Fe-bearing (6.5 mol % Fe) synthetic hydroxylclinohumite. Whereas most high-pressure studies of hydroxylclinohumite have focused on the effect of water and related OH-spectroscopic properties, the effect of incorporation of HFSE or LILE on the elastic properties of hydroxylclinohumite is not known. In addition, a thermal equation of state for hydroxylclinohumite is needed to improve mineralogical models of water-bearing phases in subducted slabs.

Here we report comparative thermal equations of state for Ti-poor and Ti-rich clinohumites of natural origin up to 28 GPa and 750 K in situ using synchrotron-based single-crystal X-ray diffraction in a diamond-anvil cell (DAC). These results expand the compositional and temperature range over which the high-pressure behavior of clinohumite can be modeled, thus improving our knowledge of how water in minerals within subducting slabs containing DHMS may extend into the mantle transition zone where melt generation provides a feedback for volatile recycling in the crust-mantle system.

2. Experimental Methods

Samples for the current study were taken from natural gem-quality clinohumite: a yellow-colored sample hereafter denoted Ti-poor, and a red-colored sample hereafter denoted Ti-rich. Electron microprobe analysis was conducted using the JEOL JXA-8230 microprobe at Peking University, operating with an acceleration voltage of 15 kV and beam current of 20 nA. The yellow-colored, Ti-poor sample has the composition of $Mg_{8.94}Ca_{0.01}Ti_{0.07}Fe_{0.01}(SiO_4)_4(OH,F)_2$, and the red-colored Ti-rich sample has the composition, $Mg_{8.78}Mn_{0.01}Ti_{0.21}Fe_{0.02}(SiO_4)_4(OH,F)_2$. Their structure was characterized by X-ray diffraction at GSECARS (Sector 13) of the Advanced Photon Source (APS), Argonne National Laboratory, beamline 13-BM-C. The results confirm that both clinohumite samples possess space group $P2_1/b$, and their lattice parameters are $a = 4.740(2)$ Å, $b = 10.235(2)$ Å, $c = 13.649(6)$ Å, $\alpha = 100.78(3)$ Å, and $V = 650.5(4)$ Å^3 for the Ti-poor sample and $a = 4.737(1)$ Å, $b = 10.247(5)$ Å, $c = 13.662(2)$ Å, $\alpha = 100.93(2)$ Å, and $V = 651.2(3)$ Å^3 for the Ti-rich sample. Based upon the lattice parameters and microprobe chemistry, the reference density (ρ_0) for the Ti-poor sample is 3.186 g/cm^3, and for the Ti-rich sample, we obtained 3.200 g/cm^3. At ambient conditions, we also screened several chips polished to ~10 μm thickness of the Ti-poor and Ti-rich clinohumite samples for sharp diffraction peaks and off-major axis orientations to be used in the high-pressure study.

For room temperature experiments we used a short symmetric-type DAC fitted with Boehler-Almax diamond anvils having 400 μm flat culets and set into seats with 76° opening. For the high-pressure and high-temperature experiments, we used a BX90 DAC (Kantor et al., 2012). Rhenium gaskets were preindented to ~40 μm thickness, and holes were drilled to ~260 μm diameter for the samples. The polished samples were loaded together into the same sample chamber along with Pt foil for pressure calibration (Fei et al., 2007). To achieve quasi-hydrostatic conditions and maintain similar pressure environments surrounding every crystal, we loaded the cells with neon as the pressure-transmitting medium using the COMPRES/GSECARS gas-loading system (Rivers et al., 2008). The BX90 DAC was equipped with an alumina ceramic heater that was coiled by two Pt wires of 20 μm diameter and ~30 cm in length. The resistance of our heater was ~2 Ω. Temperatures were determined by a K-type thermocouple attached to one of the diamond anvils.

High-pressure, single-crystal X-ray diffraction experiments on 13-BM-C used a monochromatic X-ray beam with wavelength of 0.434 Å, focused to a 15×15 μm^2 spot (Zhang et al., 2017). X-ray diffraction (XRD) patterns were recorded with a MAR165 charge-coupled device detector that was placed about 170 mm away from the sample. To obtain adequate diffraction peaks of samples we collected data at four detector

positions achieved by rotating the detector. Wide-scan and stepped-ϕ exposures were collected in a rotation range from $-90°$ to $90°$, and the typical exposure time was 1 s per degree. The diffraction images were analyzed using the ATREX/RSV software package (Dera et al., 2013). Polarization, Lorentz, and empirically determined diamond absorption corrections were applied to the peak intensities. Lattice parameters and the orientation matrix were determined in RSV. Crystal structures at high pressures were refined from the corrected intensity data with SHELXL software, facilitated by Olex2 general user interface and WinGX (Dolomanov et al., 2009; Farrugia, 2012; Sheldrick, 2007). We used the VESTA software (Momma & Izumi, 2008) to calculate the polyhedral volumes, average bond lengths, and distortions. A crystal-structure model of $Mg_9Si_4O_{18}$ that started from the $P2_1/b$ ambient pressure structure of Ottolini, Cámara, and Bigi (2000) was used as the initial model in our refinements. According to the microprobe analysis, we assumed that the M1 and M2 sites were fully occupied by Mg^{2+}, while Mg^{2+} and Ti^{4+} occupied the M3 sites; the minor content of Mn^{2+}, Ca^{2+}, and Fe were negligible in this case (Figure S1 in the supporting information). Because of the limited number of unique observations and the low-symmetry of clinohumite ($P2_1/b$), all atom positions were refined with isotropic atomic displacement parameters (ADPs). Cations occupying the same polyhedral site were set to share the same ADP values and the same fractional coordinates. All of the sites were set to full occupancy, but site occupancy factors were allowed to vary freely if more than one cation occupied the same site. Crystallographic Information Files for all the structure refinements are provided in Tables S1 and S2 in the supporting information.

3. Results and Discussion

3.1. Isothermal Equation of State

High-pressure single-crystal XRD data for both samples were collected up to ~14 GPa at room temperature. Lattice parameters of Ti-poor and Ti-rich clinohumites are summarized in Table S3. Pressure-volume data were fitted to a third-order Birch-Murnaghan equation of state (BM3-EoS) using error-weighted least squares with EoSFit7c (Angel et al., 2014). The resulting BM3-EoS parameters are as follows: $V_0 = 650.4(3)$ Å^3, $K_{T0} = 141(4)$ GPa, and $K_{T0}' = 4.0(6)$ for Ti-poor sample and $V_0 = 650.8(3)$ Å^3, $K_{T0} = 144(4)$ GPa, and $K_{T0}' = 3.6(7)$ for Ti-rich sample, respectively. The results here indicate that there is no difference in Ti content on the bulk modulus of Ti-bearing clinohumites within error. However, the BM3 K_{T0} value of this study is significantly higher than the results for Mg-pure clinohumite from Ross and Crichton (2001) with $K_{T0} = 119.4(7)$ GPa and $K_{T0}' = 4.8(6)$, or $K_{T0} = 122.2(3)$ GPa when K_{T0}' is fixed to 4.

Having established a reliable compression curve for both Ti-poor and Ti-rich clinohumites at room temperature, we next fitted the thermal equation of state parameters to the data up ~28 GPa and 750 K, also using EoSFit7c (Angel et al., 2014). Throughout the investigated P-T range, both compositions retain the monoclinic structure (space group $P2_1/b$). P-V-T data are given in Table S4. The measured unit-cell volumes as a function of pressure and temperature for both clinohumites are plotted in Figure 1, together with the isotherms calculated using the thermoelastic parameters derived from the current fits. The thermoelastic parameters $(\partial K_{T0}/\partial_T)_P$, α_T, K_0, and K_0' obtained in this study with the high-temperature BM3-EoS are as follows: $V_0 = 650.5(3)$ Å^3, $K_0 = 140(3)$ GPa, $K_0' = 4.2(5)$, $(\partial K_{T0}/\partial_T)_P = -0.040(10)$ GPa/K, and $\alpha_T = 5.1(6) \times 10^{-5}$ K^{-1} for Ti-poor clinohumite and $V_0 = 650.9(3)$ Å^3, $K_0 = 141(3)$ GPa, $K_0' = 4.1(5)$, $(\partial K_{T0}/\partial_T)_P = -0.045(11)$ GPa/K, and $\alpha_T = 5.7(6) \times 10^{-5}$ K^{-1} for Ti-rich clinohumite. We also calculated the equation of state by fixing K_0' at 4, resulting in $V_0 = 650.4(2)$ Å^3, $K_0 = 141(1)$ GPa, $(\partial K_{T0}/\partial_T)_P = -0.037(6)$ GPa/K, and $\alpha_T = 5.0(4) \times 10^{-5}$ K^{-1} for Ti-poor clinohumite and $V_0 = 650.9(2)$ Å^3, $K_0 = 142(1)$ GPa, $(\partial K_{T0}/\partial_T)_P = -0.042(6)$ GPa/K, and $\alpha_T = 5.6(4) \times 10^{-5}$ K^{-1} for Ti-rich clinohumite. Finally, we also compare the results when fixed V_0, K_0, and K_0' to the values, which, given by the P-V data fit at 300 K, result in $(\partial K_{T0}/\partial_T)_P = -0.038(6)$ GPa/K and $\alpha_T = 5.0(4) \times 10^{-5}$ K^{-1} for the Ti-poor sample and $(\partial K_{T0}/\partial_T)_P = -0.034(6)$ GPa/K with $\alpha_T = 5.3(4) \times 10^{-5}$ K^{-1} for Ti-rich clinohumite. All three methods of fitting the high-temperature BM3-EoS (refining K_0', fixing $K_0' = 4$, and fixing V_0, K_0, and K_0' from 300 K) result in equation of state parameters that are mutually equivalent within error. Thermal parameters between low and high-Ti clinohumite samples are also equivalent within error.

3.2. Axial and Polyhedral Compression

Volume compression and axial compression data of Ti-poor and Ti-rich clinohumites at high pressures are plotted in Figure 2, normalized to room pressure values. To determine the axial compressibility of a, b, and
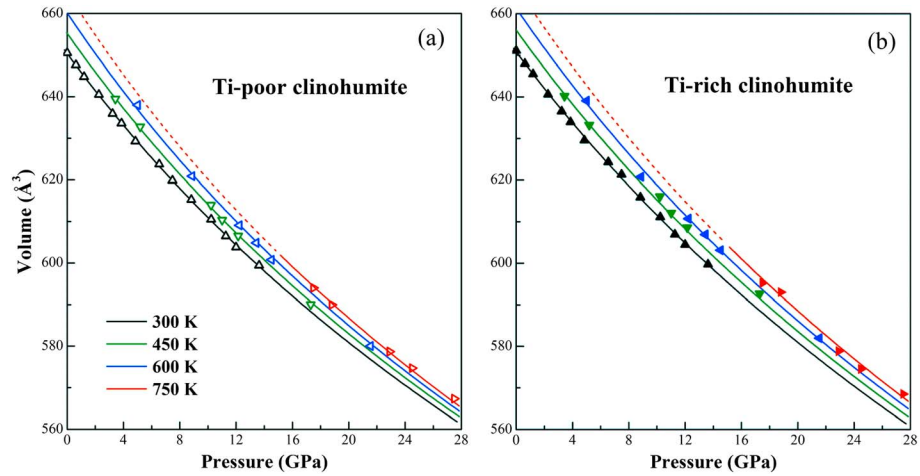
Figure 1. *P-V-T* data for (a) Ti-poor and (b) Ti-rich clinohumites obtained in this study. Isothermal compression curves at various temperatures are represented by the solid or dashed lines from the high-temperature BM EoS at 300, 450, 600, and 750 K.

c in Ti-poor and Ti-rich clinohumites, we used a linearized BM3 fitting where each axial dimension is cubed and treated as volume in the BM formulation (Angel et al., 2014). The zero-pressure axial compressibility of linear dimension *l*, defined as $\beta_{l0} = -(l^{-1})(\delta l/\delta P)_{P=0}$, is related to the linear modulus (linear incompressibility) by $M_{l0} = (\beta_{l0})^{-1}$. For Ti-poor clinohumite, our fitted linear moduli to *a*, *b*, and *c* are 591(6), 357(3), and 396(4) GPa, respectively, corresponding to axial compressibility values of $\beta_a = 1.69(1) \times 10^{-3}$, $\beta_b = 2.80(2) \times 10^{-3}$, and $\beta_c = 2.53(3) \times 10^{-3}$ GPa^{-1}. While for the Ti-rich clinohumite, we obtain linear moduli for *a*, *b*, and *c* axes of 651(8), 342(4), and 357(6) GPa, respectively, corresponding to axial compressibility values of $\beta_a = 1.54(1) \times 10^{-3}$, $\beta_b = 2.93(3) \times 10^{-3}$, and $\beta_c = 2.80(5) \times 10^{-3}$ GPa^{-1}. In both phases, there is a considerable anisotropy in axial compressibility with $\beta_b > \beta_c > \beta_a$. The ratios of zero-pressure axial compressibility in Ti-poor sample are 1.00:1.66:1.50, and for the Ti-rich sample, we find that this relationship is 1.00:1.90:1.82. The orders of axial compressibility found in this study for natural Ti-bearing clinohumites are the same as found by Ross and Crichton (2001) for synthetic Mg-pure clinohumite.
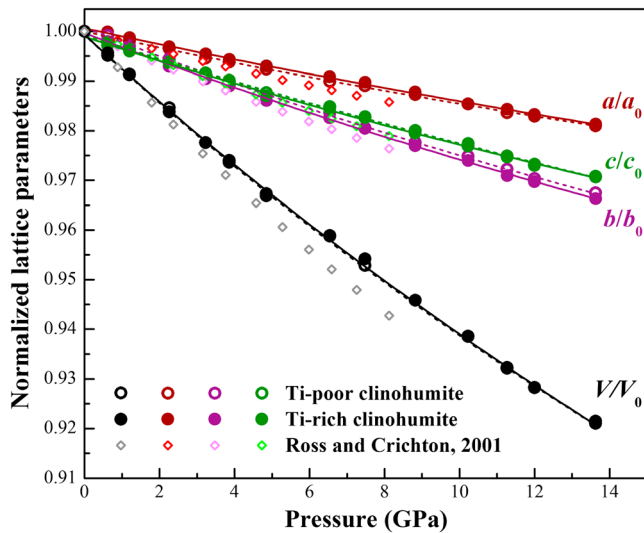
Figure 2. Normalized lattice parameters of Ti-poor and Ti-rich clinohumites as a function of pressure at room temperature. Equations of state fits in the current study are shown by dashed (Ti-poor) or solid (Ti-rich) lines.

The interaxial angle α of both samples decreases on compression, and the Ti-rich sample has a larger angle than the Ti-poor sample, which is consistent with previous result that Ti increases α (Ye et al., 2013). Here we note that the *b* and *c* axes do not belong to the principle compressional axes and the change of the axial compressibility is explained by the rotation of the strain tensor, which will be discussed next. For those minerals in monoclinic or triclinic systems with α angles that change continuously with pressure, the *b* and *c* axes of the crystal are not the directions of maximum and minimum compressions of the crystal structure, that is, the principle axes of the strain tensor. Here the orientation and magnitude of the principal strain ellipsoid between room pressure and the maximum *P* achieved ($\Delta P = 13.6$ GPa) were calculated with the win_STRAIN software, developed by R.J. Angel, modified after Ohashi (1982). The results indicate that the unit strain ellipsoid is anisotropic. In the range of 0–13.6 GPa, the axial lengths of the strain ellipsoids are $\varepsilon_1 = -0.00302$, $\varepsilon_2 = -0.002377$, and $\varepsilon_3 = -0.001934$ for Ti-poor clinohumite and $\varepsilon_1 = -0.003517$, $\varepsilon_2 = -0.002379$, and $\varepsilon_3 = -0.001977$ for Ti-rich clinohumite; both strain ellipsoids are oriented with the minor axis (ε_3) parallel to the *a* axis. The axial ratios of ε_1: ε_2: ε_3 are 1.56:1.23:1 and 1.78:1.20:1 for the Ti-poor and Ti-rich clinohumites, respectively.
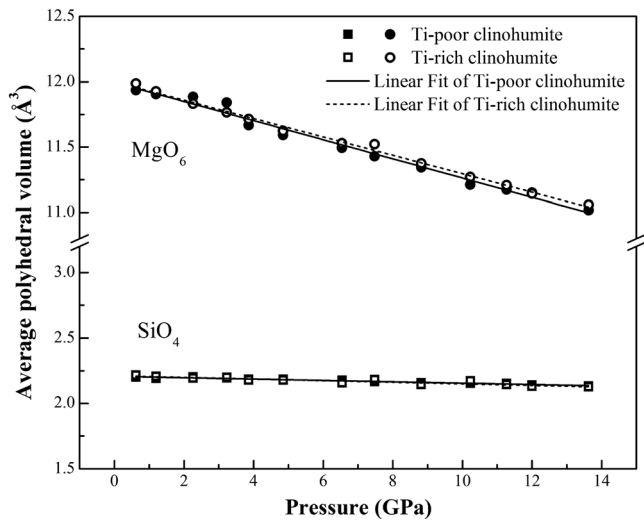
Figure 3. Pressure dependence of the average MgO_6 octahedral and SiO_4 tetrahedral volumes in Ti-poor and Ti-rich clinohumites.

We used two parameters to characterize the compression of each polyhedron: the polyhedral volume and the average bond length (Figures S2 and S3). The fractional coordinates and displacement parameters of atoms in both Ti-poor and Ti-rich clinohumites are listed in Tables S5 and S6. The crystal structure of clinohumite is illustrated in Figure S1. There are five distinct octahedral sites (Mg1A, Mg1B, Mg2A, Mg2B, and Mg3), two distinct Si tetrahedral sites (Si1 and Si2), nine O positions, and one H position. Among these two types of polyhedra, octahedra show the greatest compression, while the tetrahedra show little or no compression (Figure 3). The average MgO_6 volume is 11.96 $Å^3$ at 0.6 GPa and decreases to 11.03 $Å^3$ at 13.6 GPa in Ti-poor clinohumite, while the average octahedral volume in the Ti-rich sample is about 0.25% larger than the Ti-poor sample and changes from 11.99 to 11.06 $Å^3$ between 0.6 and 13.6 GPa. The slightly larger size of the Mg3 site in the Ti-rich clinohumite is attributed to incorporation of Ti. Between 0.6 and 13.6 GPa, the SiO_4 tetrahedra show the least compression, decreasing from 2.19 to 2.14 $Å^3$ for $Si1O_4$ and from 2.21 to 2.13 $Å^3$ for $Si2O_4$ in Ti-poor clinohumite, and from 2.20 to 2.15 $Å^3$ for $Si1O4$ and from 2.22 to 2.13 $Å^3$ for $Si2O_4$ in Ti-rich clinohumite (Figure 3). Therefore, the unit-cell volume decrease on compression is dominated by the compression of the MgO_6 polyhedra. The distortion index, bond angle variance (σ^2), and quadratic elongation (λ) are discussed in the supporting information.

In this study, both clinohumites are modeled in space group $P2_1/b$ (with a unique), which is a nonstandard setting of $P2_1/c$ chosen to preserve the structural similarity to olivine (Ye et al., 2013). The crystal structure has been described as being composed of alternating layers whose compositions can be expressed by forsterite-like blocks, $[Mg_2SiO_3(OH,F)]$ and brucite-like blocks, $[MgO(OH,F)]$ (Ribbe et al., 1968). Comparing the two compositions in this study, the $Ti_{tot} = 0.21$ pfu in Ti-rich clinohumite is about 3 times that in Ti-poor clinohumite with $Ti_{tot} = 0.07$ pfu, but we observe no significant influence on the volume and bulk modulus within uncertainties. One possible reason for this is that in order to maintain charge balance, the $Ti^{4+} \leftrightarrow Mg^{2+}$ substitution occurs coupled with $O^{2-} \leftrightarrow OH$ substitution; therefore, the size effect due to the $Ti^{4+} \leftrightarrow Mg^{2+}$ substitution (CN = 6, Mg^{2+}: 0.72 Å and Ti^{4+}: 0.605 Å) can be counterbalanced by the opposed influence of the $O^{2-} \leftrightarrow OH$ substitution (CN = 3, O^{2-}: 1.36 Å and OH^-: 1.34 Å) (Friedrich et al., 2001; Shannon, 1976).

3.3. Comparison With Previous Studies

The 300 K equation of state parameters for natural Ti-bearing clinohumites determined in this study is compared with other humite-group minerals in Figure 4 from other studies (Friedrich et al., 2002; Kuribayashi et al., 2004, 2008; Ross & Crichton, 2001). Reported values of the isothermal bulk modulus (K_{T0}) and pressure derivative (K_{T0}') of humite minerals range significantly, from ~115 to 143 GPa for K_0 and from 3 to 5.4 for K_{T0}'. Unraveling the systematic trends by structure and composition would be difficult with the limited number of different samples at the present time, but a few distinct crystal-chemical trends can be noted. All humite minerals from previous studies incorporate hydroxyl or substitute of F for OH in the structure (Friedrich et al., 2002; Kuribayashi et al., 2004, 2008; Ross & Crichton, 2001). It has been demonstrated that increasing the OH and F content makes the structure more compressible (Friedrich et al., 2002; Ross & Crichton, 2001); furthermore, this effect might be greater in chondrodite because of a greater variation in volume with F content than in clinohumite due to the greater proportion of $Mg(OH,F)_6$ octahedra in the structure (Ross & Crichton, 2001). The variation of bulk modulus with water content in
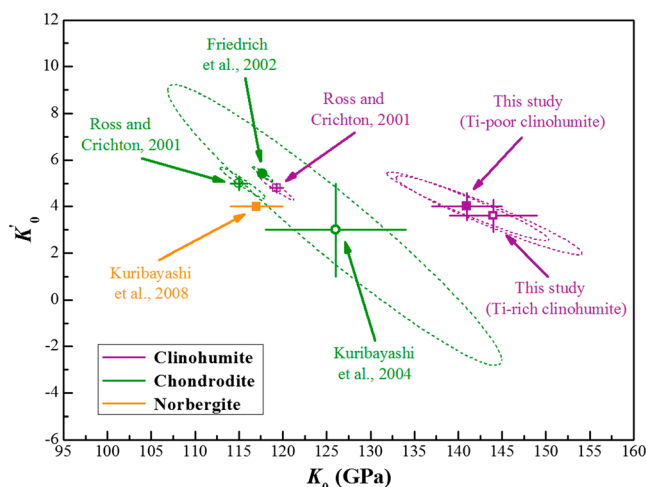
Figure 4. Isothermal bulk moduli and their pressure derivatives of minerals in the humite group, plotted as confidence ellipsoids at the 95.4% level.

humite minerals along the olivine-brucite join is roughly −2.7 GPa/wt % H_2O (Ye et al., 2015), which is significantly less than the addition of water into nominally anhydrous wadsleyite, which exhibits about −7 GPa/wt % H_2O (Chang et al., 2015). However, since the hydroxylclinohumite studied by Ross and Crichton (2001) and the current study have roughly similar water contents, the large difference in K_0 between their synthetic Mg sample and the current natural Ti-bearing samples is therefore due to other factors such as the more complex chemistry of the natural samples, which includes other impurities including Mn, Ca, and likely minor HFSEs. The main difference in composition between these natural clinohumites and synthetic Mg-clinohumite is the presence of Ti, which may be the dominant factor in causing an increase in the bulk moduli.

Ye et al. (2013) measured the thermal expansion of pure-Mg hydroxylclinohumite from 153 to 787 K at room pressure by single-crystal X-ray diffraction, and the derived volume thermal expansivity $\alpha_0(V)$ is $3.68(6) \times 10^{-5}$ K^{-1}. Our values of $\alpha_0(V)$ for natural Ti-bearing clinohumites of $5–6 \times 10^{-5}$ K^{-1} are larger well beyond standard deviation, possibly not only due to the compositional difference (natural versus Mg-pure synthetic) but also due to the difference in the fitting methods (high-temperature BM-EoS versus second-order polynomial fitting). Since our results were derived from the BM-EoS formulation, and the Ti-poor and Ti-rich clinohumites were compressed in the same DACs in this study, the fitted values of $(\partial K_{T0}/\partial_T)_P$ and α_T can be well compared internally (between Ti-poor and Ti-rich).

4. Implications for Mineralogy of Subducted Slabs

Recent seismology studies have shown the existence of low-velocity layers associated with partial melts at depths above and below the transition zone, indicating the presence of dehydration reactions and likelihood that hydrous minerals carry water into the deep mantle (Hier-Majumder & Tauzin, 2017; Liu et al., 2016; Schmandt et al., 2014). It is therefore important to include hydrous minerals in models of slab mineralogy below ~300 km depth. Clinohumites are among the few known naturally occurring hydrous phases potentially stable to conditions below 300 km, having been observed coexisting with olivine in hydrous experiments up to 12 GPa and 1200–1400°C (Smyth, 2006). In addition, subducted slabs have been proposed to be important carriers of trace elements, such as Pb, Sr, and also HFSE (e.g., Ti and Zr) (Hermann et al., 2006). Petrological evidence suggests that the OH defects are associated with the HFSE Ti in naturally occurring rocks from combined evidence of FTIR spectroscopy and TEM measurements (Hermann et al., 2006). Shen et al. (2014) studied the relation between water and Ti concentrations on olivine and humite minerals, finding that the ratio of H_2O to Ti is highest in olivine, followed by Ti-chondrodite and Ti-clinohumite. Consequently, there is expected to be a strong correlation between the Ti content of minerals and their capacity to transport water to the deeper mantle in subduction zones. Grutzner et al. (2017) showed that even small amounts of F^- substituting for OH^- are sufficient to stabilize clinohumite to temperatures well above the normal mantle geotherm and proposed that in the subducted zone, clinohumite can effectively transport water and other mass from the shallow depths to the deep as the transition zone. In this work, we have presented *P-V-T* equation of state data for natural Ti-bearing clinohumite that will improve constraints in mineralogical models of subducted slabs.

Field observations and experiments have shown that deeply metasomatized rocks such as Ti-clinohumite-bearing garnet peridotites may contribute more to sources of intraplate magmas such as kimberlites and alkali basalts because of the high volatile and HFSE concentrations, which could provide more information on the processes of slab-mantle interaction and mantle metasomatism in deep subducted slabs (Katayama et al., 2003). Furthermore, fluid-rock interactions and *P-T* variations as fluids migrate through the mantle wedge could affect the stability of some HFSE-bearing minerals, triggering the precipitation of HFSE-bearing accessory phases that are eventually recycled to the mantle and contributing to the dispersion of HFSE (Louvel et al., 2013). In eclogite-facies rocks, the presence of large ion lithophile elements (LILEs) and light rare earth (LREE)-bearing hydrous phases such as epidote and lawsonite, together with HFSE repositories and other Ti-rich minerals, control the trace element budge of evolved fluids and fluid-mediated cycling of slab components into the Earth's mantle (Scambelluri & Philippot, 2001; Schmidt & Poli, 2014).

To illustrate the physical properties of Ti-bearing clinohumite in comparison to related minerals at deep mantle conditions, the newly determined thermoelastic properties in our present study were used to plot the density ρ and bulk sound velocity V_φ profiles of both Ti-poor and Ti-rich clinohumites at 1500 K and at
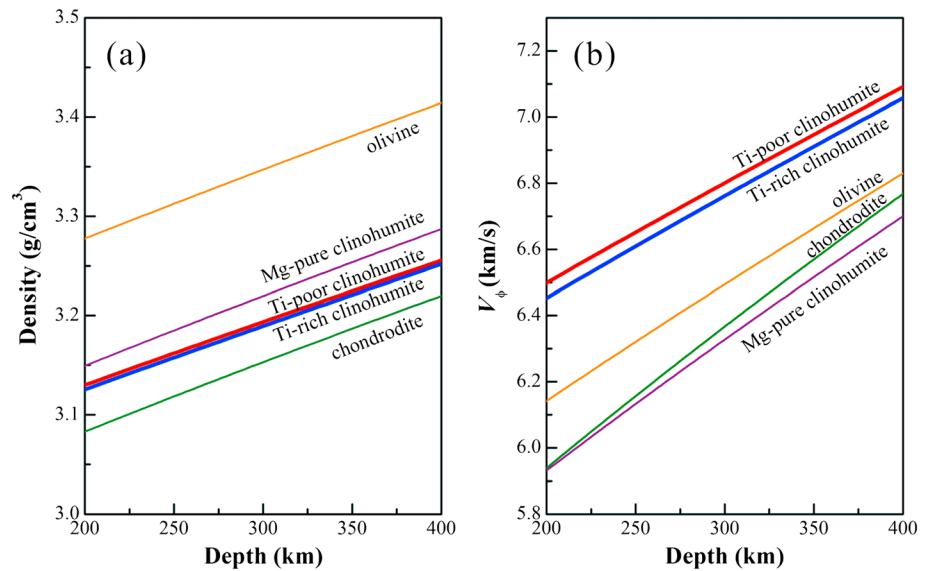
Figure 5. (a) Density and (b) bulk sound velocity profiles of Ti-poor and Ti-rich clinohumites at 1500 K between 200 and 400 km. Density and bulk sound velocity of other related minerals at deep mantle conditions are also plotted for comparison. Orange lines: olivine, $(Mg_{0.9}Fe_{0.1})_2SiO_4$ (Liu & Li, 2006); purple lines: clinohumite (Mg-pure), $Mg_9Si_4O_{16}(OH)_2$ (Ross & Crichton, 2001); green lines: chondrodite, $Mg_5Si_2O_8(OH)_2$ (Ross & Crichton, 2001); red lines: Ti-poor clinohumite, $Mg_{8.94}Ca_{0.01}Ti_{0.07}Fe_{0.01}(SiO_4)_4(OH,F)_2$ (this study); black lines: Ti-rich clinohumite, $Mg_{8.78}Mn_{0.01}Ti_{0.21}Fe_{0.02}(SiO_4)_4(OH,F)_2$ (this study).

pressures corresponding to 200–400 km depth (Figure 5). With the derived K_T and α, the V_φ can be calculated using the following equations:

$$K_S = (1 + \alpha\gamma T)K_T$$
$$V_\Phi = \sqrt{K_S/\rho}$$

where K_S is the adiabatic bulk modulus, ρ is density, γ is the thermodynamic Grüneisen parameter, and T is temperature. To calculate K_S, we used thermal expansion coefficients $\alpha_T = 5.0(5) \times 10^{-5}$ K^{-1} for Ti-poor clinohumite and $\alpha_T = 5.5(5) \times 10^{-5}$ K^{-1} for Ti-rich clinohumite from the current study, with a Grüneisen parameter, $\gamma = 1.50(4)$ (Ye et al., 2015). The densities of pure-Mg, low-Ti, and high-Ti clinohumite at 300 K and 1500 K are plotted as a function of pressure in Figure S8.

As shown in Figure 5, the calculated density of Ti-bearing clinohumites at 200–400 km and 1500 K is ~1.6% lower than the density of Mg-pure clinohumite but higher than the density of chondrodite by about ~1.1%. Olivine with forsterite-90 composition is ~4–5% denser than both clinohumites and chondrodite because of the iron incorporation into the structure. The difference in Ti content and other influence factors in natural clinohumites only produce marginal difference in density and bulk velocity between 200 and 400 km. For the bulk sound velocity, both Ti-bearing clinohumites have ~4–6% greater calculated velocity than olivine, Mg-pure clinohumite, and chondrodite. Compared with the modeled velocities of Mg-pure clinohumite (Ross & Crichton, 2001) at the P-T conditions of upper mantle, our results show that the Ti effect on elasticity of clinohumite leads to an ~5.7% and ~5.3% increase in bulk sound velocity for Ti-poor and Ti-rich clinohumites, respectively. Olivine exhibits a greater velocity than chondrodite and Mg-pure clinohumite but lower than those of in both Ti-bearing clinohumites at 200 and 400 km regions. In summary, the presence of 0.07 and 0.21 apfu Ti in Ti-bearing clinohumites slightly lowers the density but significantly increases the bulk sound velocity compared with Mg-pure clinohumite. Clinohumite can effectively transport water, other volatiles, and HFSEs from shallow depths into the transition zone of the mantle.

5. Conclusions

In summary, the high-pressure high-temperature crystal structure and equation of state of naturally occurring Ti-poor and Ti-rich clinohumites have been investigated by synchrotron-based, single-crystal XRD at

pressures up to ~28 GPa and temperatures up to 750 K. The comparative compressibility of Ti-poor clinohumite (0.07 apfu Ti) and Ti-rich clinohumite (0.21 apfu Ti) are identical within error but exhibit bulk moduli approximately 20% greater than has been found in Mg-pure clinohumite. The complex crystal chemistry of natural compositions including minor Ti, Mn, Ca, and HFSE may contribute to the difference in observed compressibility and influence the high P-T stability of humite-group minerals. In this study, no phase transitions were observed up to 28 GPa and 750 K. Thermal equation of state parameters for naturally occurring compositions of humite-group minerals will improve our ability to model the mineralogy of subducted slabs and better understand the flux of volatiles and HFSE in the crust-mantle system and their relations to melting processes and the buoyancy of subducted slabs in the Earth's mantle.

References

Angel, R. J., Alvaro, M., & Gonzales-Plates, J. (2014). EosFit7c and a Fortran module (library) for equation of state calculations. *Zeitschrift fuer Kristallographie*, *229*, 1165–1176.

Chang, Y. Y., Jacobsen, S. D., Bina, C. R., Thomas, S. M., Smyth, J. R., Frost, D. J., … Dera, P. (2015). Comparative compressibility of hydrous wadsleyite and ringwoodite: Effect of H_2O and implications for detecting water in the transition zone. *Journal of Geophysical Research: Solid Earth*, *120*, 8259–8280. https://doi.org/10.1002/2015JB012123

Dera, P., Zhuravlev, K., Prakapenka, V. B., Rivers, M. L., Finkelstein, G. J., Grubor-Urosevic, O., … Downs, R. T. (2013). High pressure single-crystal micro X-ray diffraction analysis with GSE_ADA/RSV software. *High Pressure Research*, *33*(3), 466–484. https://doi.org/10.1080/08957959.2013.806504

Dolomanov, O. V., Bourhis, L. J., Gildea, R. J., Howard, J. A., & Puschmann, H. (2009). OLEX2: A complete structure solution, refinement and analysis program. *Journal of Applied Crystallography*, *42*(2), 339–341. https://doi.org/10.1107/S0021889808042726

Faccenda, M. (2014). Water in the slab: A trilogy. *Tectonophysics*, *614*, 1–30. https://doi.org/10.1016/j.tecto.2013.12.020

Farrugia, L. J. (2012). WinGX and ORTEP for Windows: An update. *Journal of Applied Crystallography*, *45*(4), 849–854. https://doi.org/10.1107/S0021889812029111

Fei, Y. W., Ricolleau, A., Frank, M., Mibe, K., Shen, G. Y., & Prakapenka, V. B. (2007). Toward an internally consistent pressure scale. *Proceedings of the National Academy of Sciences of the United States of America*, *104*(22), 9182–9186. https://doi.org/10.1073/pnas.0609013104

Friedrich, A., Lager, G. A., Kunz, M., Chakoumakos, B. C., Smyth, J. R., & Schultz, A. J. (2001). Temperature-dependent single-crystal neutron diffraction study of natural chondrodite and clinohumites. *American Mineralogist*, *86*(9), 981–989. https://doi.org/10.2138/am-2001-8-904

Friedrich, A., Lager, G. A., Ulmer, P., Kunz, M., & Marshall, W. G. (2002). High-pressure single-crystal X-ray and powder neutron study of F,OH/OD-chondrodite: Compressibility, structure, and hydrogen bonding. *American Mineralogist*, *87*(7), 931–939. https://doi.org/10.2138/am-2002-0716

Fritzel, T. L. B., & Bass, J. D. (1997). Sound velocities of clinohumite, and implications for water in Earth's upper mantle. *Geophysical Research Letters*, *24*(9), 1023–1026. https://doi.org/10.1029/97GL00946

Grutzner, T., Klemme, S., Rohrbach, A., Gervasoni, F., & Berndt, J. (2017). The role of F-clinohumite in volatile recycling processes in subduction zones. *Geology*, *45*(5), 443–446. https://doi.org/10.1130/G38788.1

Hermann, J., Gerald, J. D. F., Malaspina, N., Berry, A. J., & Scambelluri, M. (2006). OH-bearing planar defects in olive produced by the breakdown of Ti-rich humite minerals from Babie Shan (China). *Contributions to Mineralogy and Petrology*, *153*, 417–428.

Hermann, J., Spandler, C., Hack, A., & Korsakov, A. V. (2006). Aqueous fluids and hydrous melts in high-pressure and ultra-high pressure rocks: Implications for element transfer in subduction ones. *Lithos*, *92*(3-4), 399–417. https://doi.org/10.1016/j.lithos.2006.03.055

Hier-Majumder, S., & Tauzin, B. (2017). Pervasive upper mantle melting beneath the western US. *Earth and Planetary Science Letters*, *463*, 25–35. https://doi.org/10.1016/j.epsl.2016.12.041

Hirschmann, M. M. (2006). Water, melting, and the deep Earth H_2O cycle. *Annual Review of Earth and Planetary Sciences*, *34*(1), 629–653. https://doi.org/10.1146/annurev.earth.34.031405.125211

Hirth, G., & Kohlstedt, D. L. (1996). Water in the oceanic upper mantle: Implications for rheology, melt extraction and the evolution of the lithosphere. *Earth and Planetary Science Letters*, *144*(1-2), 93–108. https://doi.org/10.1016/0012-821X(96)00154-9

Jacobsen, S. D., & Smyth, J. R. (2006). Effect of water on the sound velocities of ringwoodite in the transition zone. In S. D. Jacobsen & S. Van der Lee (Eds.), *Earth's deep water cycle* (pp. 131–145). New York: Wiley. https://doi.org/10.1029/168GM10

Kantor, I., Prakapenka, V. B., Kantor, A., Dera, P., Kurnosov, A., Sinogeikin, S., … Dubrovinsky, L. (2012). BX90: A new diamond anvil cell design for X-ray diffraction and optical measurements. *The Review of Scientific Instruments*, *83*(12), 125102. https://doi.org/10.1063/1.4768541

Karato, S. I., & Wu, P. (1993). Rheology of the upper mantle: A synthesis. *Science*, *260*(5109), 771–778. https://doi.org/10.1126/science.260.5109.771

Katayama, I., Muko, A., Lizuka, T., Maruyama, S., Terada, K., Tsutsumi, Y., … Liou, J. G. (2003). Dating of zircon from Ti-clinohumite-bearing garnet peridotite: Implication for timing of mantle metasomatism. *Geology*, *31*(8), 713–716. https://doi.org/10.1130/G19525.1

Kuribayashi, T., Kagi, H., Tanaka, M., Akizuki, M., & Kudoh, Y. (2004). High-pressure single crystal X-ray diffraction and FT-IR observation of natural chondrodite and synthetic OH-chondrodite. *Journal of Mineral ogical and Petrological Sciences*, *99*, 118–129.

Kuribayashi, T., Tanaka, M., & Kudoh, Y. (2008). Synchrotron X-ray analysis of norbergite, $Mg_{2.98}Fe_{0.01}Ti_{0.02}Si_{0.99}O_4(OH_{0.31}F_{1.69})$ structure at high pressure up to 8.2 GPa. *Physics and Chemistry of Minerals*, *35*(10), 559–568. https://doi.org/10.1007/s00269-008-0248-0

Lin, C. C., Liu, L. G., & Irifune, T. (1999). High-pressure Raman spectroscopic study of chondrodite. *Physics and Chemistry of Minerals*, *26*(3), 226–233. https://doi.org/10.1007/s002690050181

Lin, C. C., Liu, L. G., Mernagh, T. P., & Irifune, T. (2000). Raman spectroscopic study of hydroxyl-clinohumite at various pressures and temperatures. *Physics and Chemistry of Minerals*, *27*(5), 320–331. https://doi.org/10.1007/s002690050261

Liu, Z. X., Larger, G. A., Hemley, R. J., & Ross, N. L. (2003). Synchrotron infrared spectroscopy of OH-chondrodite and OH-clinohumite at high pressure. *American Mineralogist*, *88*(10), 1412–1415. https://doi.org/10.2138/am-2003-1003

Liu, W., & Li, B. S. (2006). Thermal equation of state of $(Mg_{0.9}Fe_{0.1})_2SiO_4$ olivine. *Physics of the Earth and Planetary Interiors*, *157*(3-4), 188–195. https://doi.org/10.1016/j.pepi.2006.04.003

Liu, Z., Park, J., & Karato, S. (2016). Seismological detection of low-velocity anomalies surrounding the mantle transition zone in Japan subduction zone. *Geophysical Research Letters*, *43*(6), 2480–2487. https://doi.org/10.1002/2015GL067097

Louvel, M., Sanchez-Valle, C., Malfait, W. J., Testemale, D., & Hazemann, J. L. (2013). Zr complexation in high pressure fluids and silicate melts and implications for the mobilization of HFSE in subduction zones. *Geochimica et Cosmochimica Acta*, *104*, 281–299. https://doi.org/10.1016/j.gca.2012.11.001

Mao, Z., & Li, X. Y. (2016). Effect of hydration on the elasticity of mantle minerals and its geophysical implications. *Science China Earth Sciences*, *59*(5), 873–888. https://doi.org/10.1007/s11430-016-5277-9

Momma, K., & Izumi, F. (2008). VESTA: A three-dimensional visualization system for electronic and structural analysis. *Journal of Applied Crystallography*, *41*(3), 653–658. https://doi.org/10.1107/S0021889808012016

Ohashi, Y. (1982). STRAIN: A program to calculate the strain tensor from two sets of unit-cell parameters. In R. M. Hazen & L. W. Finger (Eds.), *Comparative crystal chemistry* (pp. 92–102). New York: Wiley.

Ohtani, E. (2005). Water in the mantle. *Elements*, *1*(1), 25–30. https://doi.org/10.2113/gselements.1.1.25

Ohtani, E., Mizobata, H., & Yurimoto, H. (2000). Stability of dense hydrous magnesium silicate phases in the systems Mg_2SiO_4-H_2O and $MgSiO_3$-H_2O at pressures up to 27 GPa. *Physics and Chemistry of Minerals*, *27*(8), 533–544. https://doi.org/10.1007/s002690000097

Ottolini, L., Cámara, F., & Bigi, S. (2000). An investigation of matrix effects in the analysis of fluorine in humite-group minerals by EPMA, SIMS, and SREF. *American Mineralogist*, *85*(1), 89–102. https://doi.org/10.2138/am-2000-0110

Pearson, D. G., Brenker, F. E., Nestola, F., McNeill, J., Nasdala, L., Hutchison, M. T., … Vincze, L. (2014). Hydrous mantle transition zone indicated by ringwoodite included within diamond. *Nature*, *501*, 221–224.

Prasad, P. S. R., & Sarma, L. P. (2004). A near-infrared spectroscopic study of hydroxyl in natural chondrodite. *American Mineralogist*, *89*(7), 1056–1060. https://doi.org/10.2138/am-2004-0717

Qin, F., Wu, X., Wang, Y., Fan, D. W., Qin, S., Yang, K., … Jacobsen, S. D. (2016). High-pressure behavior of natural single-crystal epidote and clinozoisite up to 40 GPa. *Physics and Chemistry of Minerals*, *43*(9), 649–659. https://doi.org/10.1007/s00269-016-0824-7

Ribbe, P. H., Gibbs, G. V., & Jones, N. W. (1968). Cation and anion substitution in the humite minerals. *Mineralogical Magazine*, *36*, 966–975.

Rivers, M., Prakapenka, V. B., Kubo, A., Pullins, C., Holl, C. M., & Jacobsen, S. D. (2008). The COMPRES/GSECARS gas-loading system for diamond anvil cells at the Advanced Photon Source. *High Pressure Research*, *28*(3), 273–292. https://doi.org/10.1080/08957950802333593

Ross, N. L., & Crichton, W. A. (2001). Compression of synthetic hydroxylclinohumite [$Mg_9Si_4O_{16}(OH)_2$] and hydroxylchondrodite [$Mg_5Si_2O_8(OH)_2$]. *American Mineralogist*, *86*(9), 990–996. https://doi.org/10.2138/am-2001-8-905

Scambelluri, M., & Philippot, P. (2001). Deep fluids in subduction zones. *Lithos*, *55*(1-4), 213–227. https://doi.org/10.1016/S0024-4937(00)00046-3

Scambelluri, M., & Rampone, E. (1999). Mg-metasomatism of oceanic gabbros and its control on Ti-clinohumite formation during eclogitization. *Contributions to Mineralogy and Petrology*, *135*(1), 1–17. https://doi.org/10.1007/s004100050494

Schmandt, B., Jacobsen, S. D., Becker, T. W., Liu, Z. X., & Dueker, K. G. (2014). Dehydration melting at the top of the lower mantle. *Science*, *344*(6189), 1265–1268. https://doi.org/10.1126/science.1253358

Schmidt, M. W., & Poli, S. (2014). *Devolatilization during subduction*, *Treatise on geochemistry* (pp. 669–701). Amsterdam: Elsevier.

Shannon, R. D. (1976). Revised effective ionic radii and systematic studies of interatomic distances in halides and chalcogenides. *Acta Crystallographica Section A*, *32*(5), 751–767. https://doi.org/10.1107/S0567739476001551

Sheldrick, G. M. (2007). A short story of SHELX. *Acta Crystallographica*, *64*(Pt 1), 112–122. https://doi.org/10.1107/S0108767307043930

Shen, T. T., Hermann, J., Zhang, L. F., PadrÓn-Navarta, J. A., & Chen, J. (2014). FTIR spectroscopy of Ti-chondrodite, Ti-clinohumite, and olivine in deeply subducted serpentinites and implications for the deep water cycle. *Contributions to Mineralogy and Petrology*, *167*(4), 992. https://doi.org/10.1007/s00410-014-0992-8

Smyth, J. R. (2006). Hydrogen in high pressure silicate and oxide mineral structures. *Reviews in Mineralogy and Geochemistry*, *62*(1), 85–115. https://doi.org/10.2138/rmg.2006.62.5

Ye, Y., Jacobsen, S. D., Mao, Z., Duffy, T. S., Hirner, S. M., & Smyth, J. R. (2015). Crystal chemistry, thermal expansion, and elasticity of OH-chondrodite: Trends among dense hydrous magnesium silicates. *Contributions to Mineralogy and Petrology*, *169*(4), 43. https://doi.org/10.1007/s00410-015-1138-3

Ye, Y., Smyth, J. R., Jacobsen, S. D., & Goujon, C. (2013). Crystal chemistry, thermal expansion, and Raman spectra of hydroxyl-clinohumite: Implications for water in Earth's interior. *Contributions to Mineralogy and Petrology*, *165*(3), 563–574. https://doi.org/10.1007/s00410-012-0823-8

Yoshino, T., Matsuzaki, T., Shatskiy, A., & Katsura, T. (2009). The effect of water on the electrical conductivity of olivine aggregated and its implications for the electrical structure of the upper mantle. *Earth and Planetary Science Letters*, *288*(1-2), 291–300. https://doi.org/10.1016/j.epsl.2009.09.032

Zhang, D. Z., Dera, P., Eng, P. J., Stubbs, J. E., Zhang, J. S., Prakapenka, V. B., & Rivers, M. L. (2017). High pressure single crystal diffraction at PX^2. *Journal of Visualized Experiments*, *119*(119), e54660. https://doi.org/10.3791/54660